The fluid dynamics of symmetry and momentum transfer in microchannels within co-rotating discs with discrete multiple inflows

Sayantan Sengupta, and Abhijit Guha

Citation: Physics of Fluids **29**, 093604 (2017); doi: 10.1063/1.5001252
View online: http://dx.doi.org/10.1063/1.5001252
View Table of Contents: http://aip.scitation.org/toc/phf/29/9
Published by the American Institute of Physics

The fluid dynamics of symmetry and momentum transfer in microchannels within co-rotating discs with discrete multiple inflows

Sayantan Sengupta and Abhijit Guha[a)]
Mechanical Engineering Department, Indian Institute of Technology Kharagpur, Kharagpur 721302, India

(Received 28 March 2017; accepted 19 August 2017; published online 21 September 2017)

This paper presents a systematic computational study of the flow in a shrouded rotor cavity (with depth of the order of 100 μm) with multiple discrete inflows revealing the physics of how an initially non-axisymmetric flow evolves, both in the Lagrangian and Eulerian frameworks, towards axisymmetry. The approach to axisymmetry happens faster for the tangential velocity as compared to the radial component. The non-uniform inlet condition for the radial and tangential velocities, consisting of high velocity at the inlet openings and zero velocity on the shroud wall in between two consecutive inlets, gives rise to an oscillatory variation in the velocity of a fluid particle, with progressively decreasing amplitude, if one tracks its motion along a surface streamline. The rate of decay of the amplitude increases, i.e., equivalently the approach to the axisymmetric condition happens at a greater radial location, as the number of inlets, N_{inlet}, is increased. When the rotational speed of the discs, Ω, is increased, the distribution of radial velocity (U_r) is significantly altered, which may result even in a change of the fundamental shape of its z-profile, changing from parabolic to flat to W-shaped. The fluid has to negotiate with two different non-uniformities within a short radial distance (Δ_{rc}): one in the θ–direction because of the presence of discrete inlets and the other in the z–direction due to the no-slip condition on the disc surface. An increase in Δ_{rc} from zero to a finite value assists in the attainment of the axisymmetric condition for both tangential and radial velocities, i.e., the axisymmetry is obtained at a larger radial location. The subtle and complex fluid dynamics of the approach to axisymmetry is comprehensively analysed by following the progressive development of the z-profiles of U_r along a surface streamline located on the middle-plane of the inter-disc-spacing for an eight-inlet flow-configuration. Two sets of velocity profiles are recorded—the first set at points whose azimuthal positions are directly aligned with the inlets and the second set at points which fall in the middle of two consecutive inlets. Both sets are of W-shape near the disc periphery, then they become flat in the middle, finally becoming parabolic. The velocity profiles of the two sets approach each other and finally become superposed when axisymmetry is attained. *Published by AIP Publishing.* https://doi.org/10.1063/1.5001252

I. INTRODUCTION

The study of the flow through co-rotating discs has attracted the attention of fluid dynamicists and engineers for its fundamental value and practical utility. A few examples of practical devices containing rotating discs are Tesla disc turbine, disc pump, centrifugal microfluidic systems (e.g., lab-on-a-disc or lab-on-a-CD), micro heat sink, computer disc memory, centrifuges, gear, rotating air cleaner, and wet clutches. In the literature, a number of papers on axisymmetric inflow through co-rotating discs,[1–7] elucidating various flow features and interesting flow physics within the rotor, are available. For example, the roles of various forces (viz., inertia, Coriolis, centrifugal and viscous) are delineated in Ref. 3; the mechanism of work transfer is established in Ref. 2; the physics of pressure variation is described in Ref. 1. In the present work, we explore the fluid dynamics that originates from the practical implementation of an inflow at the periphery of co-rotating discs due to the interaction of a rotating cavity, a stationary shroud, and multiple discrete inlets. The fluid dynamics in the radial clearance space Δ_{rc} between the rotating discs (of radius r_d) and the stationary shroud (situated at radius r_i) is complex since the fluid has to negotiate with two different non-uniformities within a short radial distance (Δ_{rc}). At $r = r_i$, a source of non-uniformity is present in the θ–direction, depending on the number and arrangement of the discrete inlets in the circumferential plane of the stationary shroud. At $r = r_d$, a z–directional non-uniformity exists due to the presence of two closely spaced disc-surfaces (on which the boundary condition $U_\theta = \Omega r$ is imposed as a result of no slip, where U_θ is the absolute tangential velocity, Ω is the rotational speed of the discs, and r is the radial coordinate). The non-uniform inlet condition for the radial and tangential velocities, consisting of high velocity at the inlet openings and zero velocity on the shroud wall in between two consecutive inlets, gives rise to an oscillatory variation in the velocity of a fluid particle if one tracks its motion along a spiral surface streamline. The amplitude of the fluctuations progressively decreases; this

a)Author to whom correspondence should be addressed: a.guha@mech.iitkgp.ernet.in

feature in the Lagrangian description is directly related to the approach to axisymmetric condition in the Eulerian description of the velocity field within the inter-disc spacing. The paper establishes the fluid dynamics of this progressive three-dimensional evolution of the initially non-uniform flow field toward axisymmetry.

The rotor comprises a stack of flat, parallel, coaxial discs which are closely spaced (of the order of 100 μm). The rotor is enclosed by a stationary shroud. A small radial clearance is maintained between the stationary shroud and the rotor. The shroud-wall, accommodating multiple discrete inlets, is discontinuous. Each of the inlets occupies only a small portion ($\sim 2° - 6°$) of the whole periphery (i.e., 360°) of the rotor. Through the inlet-openings, working fluid is injected nearly tangentially into the small passage between the stationary shroud and the rotor. Due to a non-zero (inward) radial velocity component, the fluid in this narrow passage enters into the inter-disc-spacings (of the order of 100 μm) and approaches towards the exhaust port located at the centre of each disc.

The flow in shrouded co-rotating discs has been discussed by a number of researchers, and many flow features are explained in Refs. 8–12. Abrahamson *et al.*, in their experimental investigation with shrouded co-rotating discs,[8] observed three distinct regions of flow, viz., an inner region near the hub acting as a solid-body, an outer region dominated by large counter-rotating vortices, and a boundary layer region on the shroud. Huang and Hsieh[10] employed particle image velocimetry (PIV) and observed five characteristic regions (solid-body rotation region, hub-influenced region, buffer region, vortex region, and shroud-influenced region). Wu[11] also employed PIV and quantitatively identified the shroud-influenced region. The knowledge acquired from the study of flow between shrouded co-rotating discs helps one to understand the aerodynamics of hard disc drives (HDD). Hendriks[13] studied the flow-induced vibration (FIV) of discs in HDD by computational fluid dynamics (CFD) simulations; and, Shirai *et al.*[14] performed experiments on FIV in HDD. The present flow configuration is different from the configurations considered in Refs. 8–14. In Refs. 8–14, the fluid is driven by the rotational motion of the discs, whereas, in the flow configuration discussed in the present paper, the fluid drives all disc-surfaces. In the transient starting-up process, the tangential momentum of the fluid coming out of the inlet (nozzle) applies a drag force, because of the no slip boundary condition, on the surfaces of the initially static discs and the discs start rotating with an angular acceleration. What final steady rotational speed Ω is attained by the discs depends on the load applied on the shaft connected to the discs. Instead of modelling the transient starting-up process, here we try to determine the steady state solution directly. For this, the inlet flow conditions and the rotational speed Ω of the discs are specified at the respective boundaries, and the steady state flow solutions are obtained. At the steady state, the loss of angular momentum by the fluid between the inlet and the outlet is equal in magnitude to the integrated torque applied by the shear stress acting on the disc surfaces. The so determined power output from the steady flow simulations is the same as the above-mentioned load for which the discs, being driven by the fluid, would have attained the same rotational speed Ω asymptotically at the end of the transient starting-up process.

Another differentiating aspect of the present study (as compared to Refs. 8–14) is that there is a superposed inward flow by discrete multiple nozzles set at the periphery of the shrouded discs. The presented three-dimensional flow field, which is non-uniform in r, θ, and z directions, is useful for comprehending the fluid dynamics within a Tesla disc turbine invented and patented[15] by the famous scientist Nikola Tesla. Most theoretical studies of Tesla disc turbines assume axisymmetric inlet condition at the periphery of the rotor. Many practical implementations, on the other hand, employ discrete nozzles at the rotor periphery. This paper is intended to bridge this gap by providing a systematic study of the interaction of discrete multiple inflows with the rotor consisting of closely spaced co-axial discs. Such a study is interesting from a fundamental point of view, and the present work focuses on establishing physical understanding of the fluid dynamics. The fluid dynamics eventually has important implication for the performance of any engineering device utilizing the flow configuration considered. [Continued (as yet unpublished) work by the present authors, for example, has shown that the efficiency of the Tesla disc turbine can be increased very significantly by increasing the number of nozzles and that the highest efficiency is obtained when axisymmetric boundary condition can be established at the rotor inlet (i.e., at the outer periphery).] Such considerations of the role of flow symmetry on the performance of any specific engineering device are, however, not included in this work. (Many aspects of performance of a Tesla disc turbine are discussed in Refs. 16–18.)

According to Czarny *et al.*,[19] while the geometry may be strictly axisymmetric, it is possible to have non-axisymmetric patterns for turbulent (and unstable) flow adjacent to rotating discs. Several studies are available in the literature dealing with non-axisymmetric flow in an axisymmetric geometric-configuration formed by parallel, coaxial discs. Czarny *et al.*[19] showed non-axisymmetric flow patterns in a rotor-stator disc cavity; Nore *et al.*[20] showed non-axisymmetric flow patterns between exactly counter-rotating discs; and, Hewitt and Al-Azhari[21] found non-axisymmetric flow between two independently rotating infinite, parallel discs. In Refs. 19–21 non-axisymmetry arises due to turbulent flow. We, however, consider laminar flow. Non-axisymmetry, in the present study, arises due to the presence of a stationary shroud and discrete inlets in the flow configuration.

The complex interaction of the discrete multiple inflows within the small radial clearance space between the shroud and the rotor, the three-dimensional spatial evolution during the subsequent flow through the rotor-rotor cavity, and the attainment of a nearly axisymmetric distribution towards the outlet have been investigated in this paper. We examine the effects of the number of inlets (N_{inlet}), the rotational speed of the discs (Ω), and the radial clearance between the rotor and the shroud (Δ_{rc}) on the fluid dynamics of flow through the rotating cavity. In order to capture the physics thoroughly, fully three-dimensional CFD simulations are performed on a fine grid, which is necessary to capture the fluid dynamics at a small scale inside the clearance space. Each CFD simulation is run to a high degree of convergence (maximum RMS residual being 10^{-6}). The CPU time for each simulation varied from about 4 h to about 32 h, run on a cluster (x86-64 architecture and 198 GB RAM) of 16 processors [Intel(R) Xeon(R) CPU E5-4640 with base frequency of 2.40 GHz].

II. METHOD OF CFD SIMULATION

The compressible Navier-Stokes equations are solved by a commercially available CFD software CFX 15.[22] In our earlier related work,[1,2,18] we used the incompressible formulation. For the present work with discrete inflows, the local Mach number in certain cases is such that the compressibility effect may be relevant. For example, the maximum local Mach number is 0.35 for $N_{inlet} = 4$, and the maximum local Mach number is 0.66 for $N_{inlet} = 2$. Thus the energy equation is included in the present simulations to account for the compressibility effect wherever necessary. (This increased the requirement for computational resources and the CPU time, but both were affordable for the present exploratory study.) The governing equations are as follows:
continuity equation,

$$\frac{\partial \rho}{\partial t} + \nabla \cdot \left(\rho \vec{U}\right) = 0, \qquad (1)$$

momentum equation,

$$\frac{\partial \left(\rho \vec{U}\right)}{\partial t} + \nabla \cdot \left(\rho \vec{U} \otimes \vec{U}\right) = -\nabla p + \nabla \cdot \tau, \qquad (2)$$

energy equation,

$$\frac{\partial \left(\rho h_t\right)}{\partial t} - \frac{\partial p}{\partial t} + \nabla \cdot \left(\rho \vec{U}\, h_t\right) = \nabla \cdot (\lambda\, \nabla T) + \nabla \cdot \left(\vec{U} \cdot \tau\right), \qquad (3)$$

where $\vec{U}$ is the velocity vector, p is the static pressure, and T is the temperature. τ is the stress tensor, which is expressed as follows:

$$\tau = \mu \left(\nabla \vec{U} + (\nabla \vec{U})^T - \frac{2}{3} \delta\, \nabla \cdot \vec{U}\right). \qquad (4)$$

In Eq. (3), $\nabla \cdot \left(\vec{U} \cdot \tau\right)$ represents the viscous work term, i.e., the work done due to viscous stresses. h_t is the total enthalpy, which is related to the static enthalpy $h(T, p)$ by $h_t = h + \vec{U}^2/2$. The effect of gravity is neglected in the analysis.

Air is used as working fluid. The dynamic viscosity μ, thermal conductivity λ, and constant pressure specific heat capacity c_p are considered to be constant. The values of μ, λ, and c_p used here are adopted for a reference state (at 25 °C and 1 atmospheric pressure). The density of air, ρ, is modelled by the equation of state for an ideal gas. The equation of state for an ideal gas is as follows:

$$\rho = p_{abs}/RT, \qquad (5)$$

where p_{abs} is the absolute pressure (the gauge pressure being denoted by p) and R is the specific gas constant of air (the ratio of the universal gas constant and the molecular weight of air).

CFX 15 is a finite volume solver. Navier-Stokes equations [Eqs. (1)–(4)] are solved for finite volumes which are generated by discretizing the spatial domain into a mesh of discrete nodes. The solver uses co-located grid, and therefore special techniques proposed by Rhie and Chow[23] are implemented to avoid the formation of a decoupled (checker-board) pressure field. The implicit formulation[24] is used. Shape functions are employed to evaluate spatial derivatives for all the diffusion terms and to calculate the velocity and pressure at integration points from the velocity and pressure at mesh nodes. The high resolution scheme,[22] whose spatial order may vary between one and two, is utilized to evaluate the advection terms at the integration points. The coupled solver, which solves the equations (for U_x, U_y, U_z, p, etc.) as a single system, is used for the simulations. Double precision arithmetic is adopted for all numerical calculations given in this paper.

It is already mentioned that the rotor consists of a stack of discs (generally 10–20 discs). Instead of solving the flow field for the full rotor, we have considered only two discs of the full rotor assuming that the flow characteristics between any two discs of the rotor are the same. This assumption is not strictly applicable in the region between the end discs and the casing where the flow field is similar to the flow field within a stator-rotor. However, the effect of the end-discs on the overall fluid dynamics and torque generation is not significant when the number of discs is large. The computational domain, comprising two discs, is shown in Fig. 1. The lower disc is at $z = 0$, and the upper disc is at $z = b$ where b is the inter-disc-spacing. Each disc has an outer radius r_d and inner radius r_o (the subscript o denotes the location of the outlet). Both the shroud-wall and the discrete inlets are located at the same circumferential plane which is at a radius r_i. The subscript i denotes the inlet. A small radial clearance is maintained between the discs and the circumferential plane containing the shroud-wall and the discrete inlets. The radial clearance Δ_{rc} equals $(r_i - r_d)$. In the present CFD simulations, the geometric parameters r_d, r_o, and b are fixed; their values being r_d = 25 mm, r_o = 13.2 mm, and b = 300 μm. The value of r_i is varied by varying Δ_{rc}. The objective is to investigate the effect of Δ_{rc} when the rotor-size is fixed. The azimuthal extent covered by each inlet is 4°. The allocation of the inlets is such that they divide the shroud-wall into a finite number of identical parts. For example, in a four-inlet configuration,

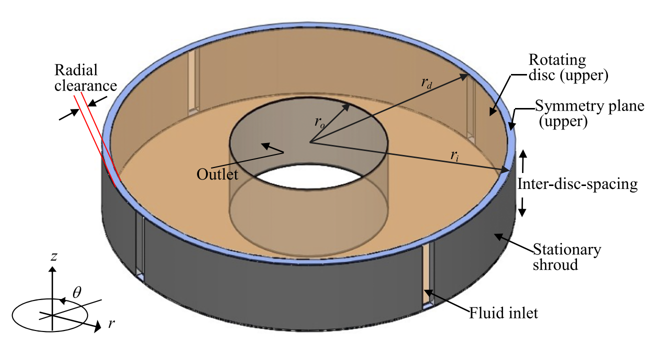

FIG. 1. Schematic diagram of the computational domain between two co-rotating discs. (The inter-disc-spacing, in relation to the radius, is exaggerated in the sketch for clarity.)

the inlets divide the shroud-wall into four identical parts (see Fig. 1).

The CFD simulations are performed for the following boundary conditions. (i) At inlets, mass flow rate ($\dot{m}$), flow angle (α_i), and total temperature (T_t) are specified. The study is conducted for a constant value of mass flow rate through the outlet ($\dot{m}_o = 3 \times 10^{-5}$ kg/s/rotating channel); each inlet is assumed to inject identical amount of mass flow rate; therefore, $\dot{m}_i = \dot{m}_o / N_{inlet}$. Unless otherwise specified, we consider $T_{t,i} = 313$ K and $\alpha_i = 6°$ with the tangential direction. Due to nonzero α_i, the velocity vector at the inlet has tangential and radial components denoted, respectively, by U_θ and U_r. (The symbol U denotes the absolute velocity and the symbol V denotes the relative velocity.) (ii) At the outlet, the gauge value of static pressure is zero. (iii) No slip condition is specified at the stationary wall of the shroud. (iv) No slip condition is set on the disc surfaces (upper and lower). A rotational speed Ω of the disc-surface is also set. (v) The circular strips (upper and lower) extended from r_d to r_i are modelled by the "symmetry" boundary condition. The circular strip is shown in Fig. 1.

We present the CFD solutions for steady, laminar, subsonic flow (the maximum local Mach number is 0.66). To maintain laminar flow, the dynamic similarity number Ds ($Ds \equiv |U_{r,i}| b^2/\nu\, r_i$) is kept below 10,[2,3] where, $|U_{r,i}|$ is the radial velocity at the inlet and ν is the kinematic viscosity of the working fluid. The value of the maximum Reynolds number based on the local radial velocity at $r = r_i$ (i.e., $|U_{r,i}| b/\nu$) is 547 (which occurs for the two-inlet configuration). The value of the maximum Reynolds number based on the area-averaged radial velocity at $r = r_i$ (i.e., $|\bar{U}_{r,i}| b/\nu$) is 12.7.

Grid-independence test has been carried out separately for each flow configuration (i.e., for each value of N_{inlet}). Table I and Fig. 2 show a few pertinent details for $N_{inlet} = 4$, overall features of the grids for other values of N_{inlet} being summarized in Table II. We have used mapped, hexahedral computational cells for the results presented in this paper. The grids are distributed differently in the r, θ, and z directions in accordance with the difference in the flow physics in the three directions. The grid distribution in the z-direction is non-uniform with very small grid size close to the surfaces of the two discs (to capture the velocity gradient on the surface accurately) and with progressively larger grid size as one moves away from the surfaces to the middle of the inter-disc gap (with a successive ratio of 1.05). Between two consecutive inlets, the grids in the θ-direction are non-uniformly distributed. Very small grid is used at the junction of any inlet and its adjacent shroud-wall. The grid-size, starting from the end of a particular inlet, increases progressively along the shroud-wall, attains a maximum value in the midway, and then decreases progressively in the vicinity of another inlet. Uniform grid

TABLE I. Grid independence test (for $N_{inlet} = 4$, $\dot{m}_o = 30$ mg/s, $\Omega = 2000$ rad/s, $\alpha_i = 6°$, $T_{t,i} = 313$ K, $\Delta_{rc} = 0.2$ mm).

Grid distribution	Number of grids in r, θ, and z directions	Total number of cells	Area-averaged p [gauge value] at any of the four inlets (Pa)
Coarse	(130 × 220 × 40)	1 144 000	1345
Standard	(208 × 340 × 60)	4 243 200	1317
Fine	(270 × 400 × 75)	8 100 000	1312

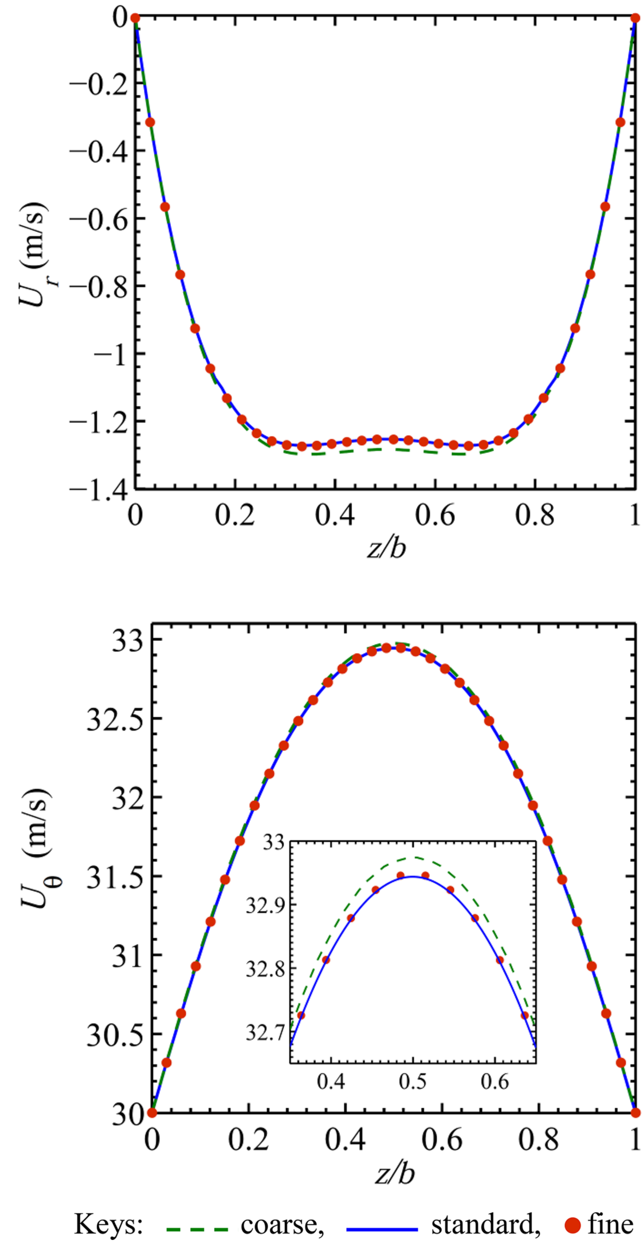

FIG. 2. The attainment of the grid independent velocity profiles by grid refinement simultaneously in r, θ, and z directions. (Simulations are performed for $N_{inlet} = 4$, $\dot{m}_o = 30$ mg/s, $\Omega = 2000$ rad/s, $\alpha_i = 6°$, $T_{t,i} = 313$ K, $\Delta_{rc} = 0.2$ mm. z-profiles of U_r and U_θ are displayed at $r = 15$ mm and $\theta = 0°$. Details of coarse, standard, and fine grid distributions for $N_{inlet} = 4$ are given in Table I.)

TABLE II. Details of fine grid distributions for various flow configurations.

Flow configuration	Total number of cells	Number of grids in r, θ, and z directions
2-inlet	10 432 800	(322 × 360 × 90)
4-inlet	8 100 000	(270 × 400 × 75)
8-inlet	6 489 600	(208 × 520 × 60)

distribution is taken within the small azimuthal extent (i.e., 4°) of any inlet. In the r-direction, the grids are divided into two zones—non-uniform and uniform.

In order to capture the boundary layers attached to the stationary shroud and the rotating discs, very small grid-size is used near the inlet, and the grid distribution is non-uniform near the inlet. The rest of the radial extent up to the outlet is meshed uniformly. Table I indicates that after attaining the standard grid distribution, any further grid refinement results in only small changes of the output parameters. We, however, present the results obtained for the fine grid distribution (Table II) in Sec. III.

III. RESULTS AND DISCUSSION

This section is divided into three subsections. Section III A shows the effect of increasing the number of inlets N_{inlet} on the fluid dynamics of the present physical configuration. Section III B provides the effect of increasing the rotational speed of the discs Ω. Section III C demonstrates the effect of the radial clearance Δ_{rc} on the velocity distributions. This section also illustrates the fluid dynamics within the radial clearance space between the shroud and rotor.

A. Effect of increasing the number of inlets (N_{inlet})

In this section, we investigate the effect of increasing the number of inlet-nozzles (N_{inlet}) on the distributions of velocity and pressure keeping all other input parameters, viz., $\dot{m}_o$, Ω, α_i, $T_{t,i}$, and Δ_{rc}, fixed. In Fig. 3, the contours of radial velocity U_r, absolute tangential velocity U_θ, and static pressure p, for 2-inlet ($N_{inlet} = 2$), 4-inlet ($N_{inlet} = 4$), and 8-inlet ($N_{inlet} = 8$) configurations, are shown. The contours are shown on the middle-plane of the inter-disc-spacing (i.e., at $z = b/2$).

If one moves along a radial line, it is found that U_r (for any nozzle-configuration) at first decreases from its large value at the inlet openings, finally increasing again near the rotor exit. This flow feature is consistent with the equation of continuity. Each inlet occupies only a small azimuthal extent (i.e., 4°).

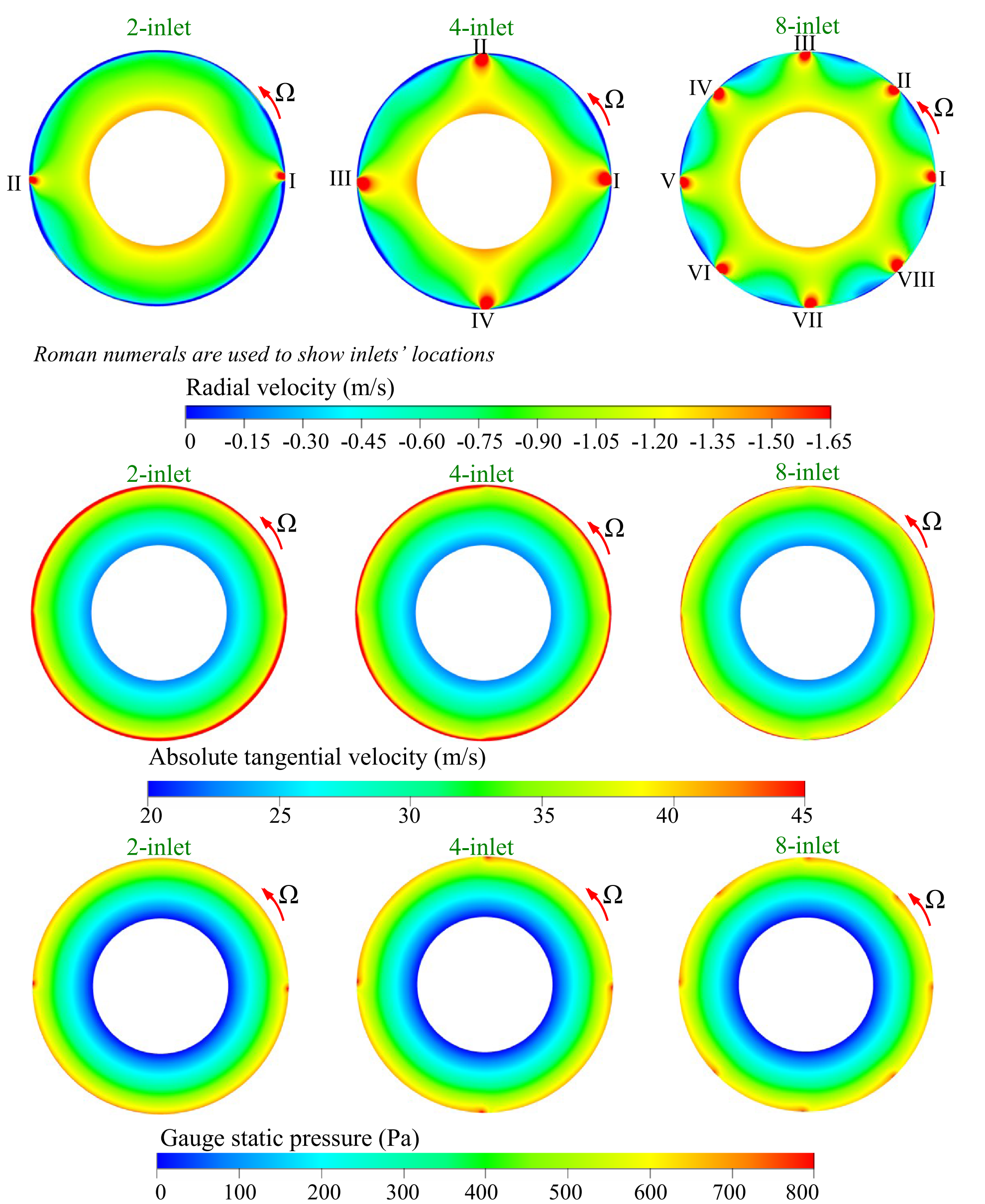

FIG. 3. Distributions of absolute tangential and radial velocities and static pressure on the middle-plane of the inter-disc-spacing (i.e., on $z = b/2$) for three different flow configurations, viz., 2-inlet, 4-inlet, and 8-inlet configurations, excluding the solution in the radial clearance space ($\dot{m}_o$ = 30 mg/s, Ω = 1500 rad/s, α_i = 6°, $T_{t,i}$ = 313 K, Δ_{rc} = 0.2 mm. The same scales are used for a given flow variable to understand how the flow asymmetry depends on the number of discrete inlet-nozzles; the minimum or maximum of scales shown here does not represent the minimum or maximum of a flow variable in any inlet configuration. As an example, the value of $U_{r,i}$ for a 2-inlet configuration is –25 m/s; if we include this value in the contour plots, then the fine details of flow asymmetry shown in this figure cannot be revealed).

Therefore, in any particular configuration, the sum of the azimuthal extents covered by all the inlets is much less than 360°. For example, for a 4-inlet configuration, this sum is only 16°. In other words, the circular boundary at $r = r_i$ is mostly occupied by the solid shroud-wall. As the fluid moves slightly inward from $r = r_i$, the full 360° extent is available for the fluid flow due to the absence of the shroud wall. This is why the magnitude of radial velocity has to decrease to satisfy the equation of continuity. The decrease of $|U_r|$ is therefore attributed to an effort of relaxing the azimuthal non-uniformity imposed at $r = r_i$. We now explain why $|U_r|$ increases towards the exit. For $r < r_i$, the available flow area, proportional to r, decreases towards the outlet. The effect of decreasing flow area counteracts the effect of azimuthal spreading near the inlet. This is why, below a certain radius, $|U_r|$ increases for any further decrease in radius. When other input parameters are fixed, non-axisymmetry decays faster with increasing N_{inlet}. This feature is demonstrated while comparing the U_r-distribution for an 8-inlet configuration with the U_r-distribution for a 2-inlet configuration (Fig. 3).

Figure 3 shows that the near-axisymmetry in the contours of U_θ and p is obtained at a larger radial location, as compared to that in the contours of U_r. This characteristic can be explained in the following way. Consider a relative frame of reference, in which an observer is rotating at the same angular speed as the discs' rotational speed (Ω). The relative tangential velocity is denoted by V_θ. The relation between the absolute and relative components of tangential velocity is as follows:

$$U_\theta = V_\theta + \Omega r. \tag{6}$$

Out of the two components of U_θ, Ωr is independent of θ. The non-axisymmetry displayed in the contour plot of U_θ is solely due to the non-axisymmetric distribution of V_θ. For the adopted geometry and input parameters, V_θ decreases substantially near the inlet, and Ωr becomes the dominant part of U_θ. Although the non-axisymmetry in V_θ persists much longer along the flow path, (the relative measure of) axisymmetry in U_θ is approached much earlier (i.e., at a larger radial location) due to the contribution of Ωr. Figure 3 shows that axisymmetry in the static pressure tends to be established more readily (i.e., occurs at a greater radial location closer to the inlet) as compared to the radial velocity component. In this regard, it should be mentioned that the boundary condition of uniform static pressure is applied at the outlet (no such boundary condition is applied on the radial or relative tangential velocity at the outlet).

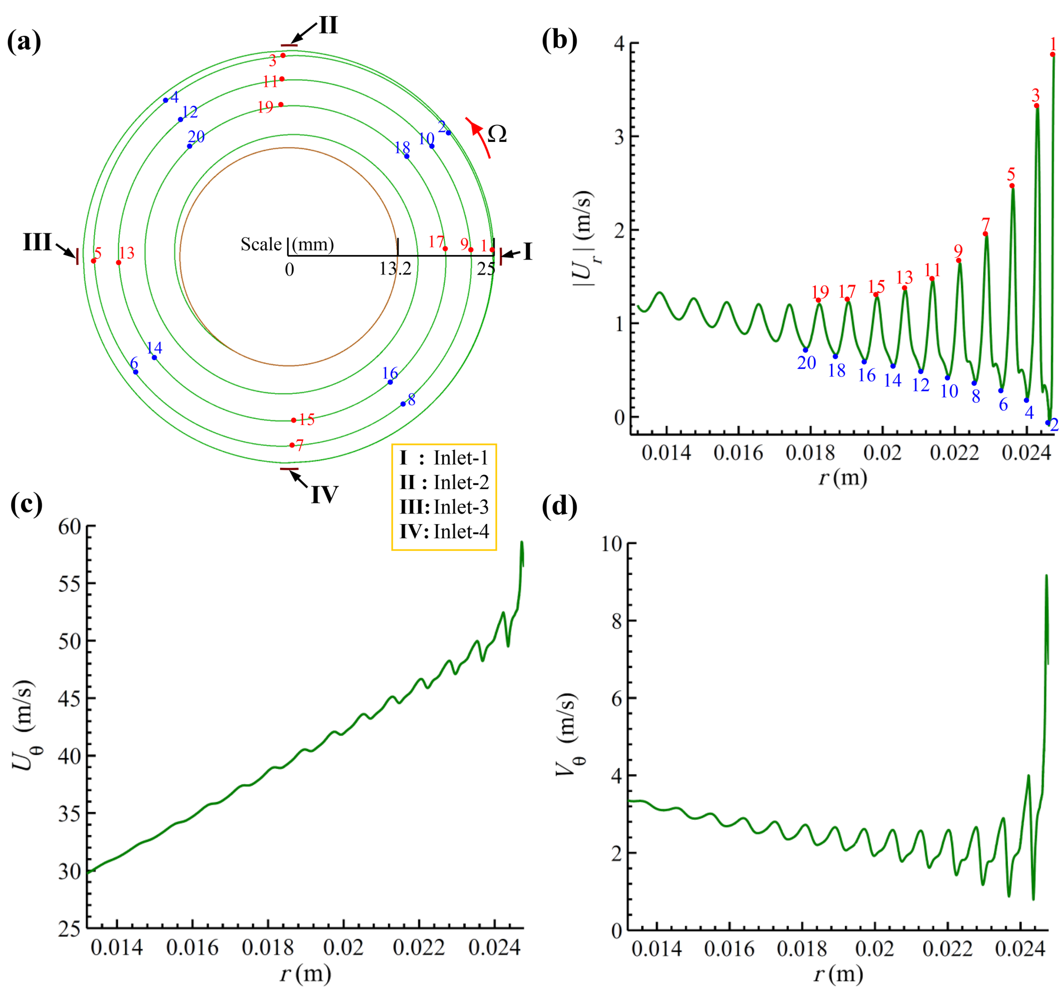

FIG. 4. Attainment of axisymmetry along a surface streamline located on the middle-plane of the inter-disc-spacing (i.e., on $z = b/2$) for a four-inlet flow-configuration. (a) A surface streamline extending from r_d to r_o; (b) the magnitude of radial velocity along the surface streamline; (c) tangential velocity along the surface streamline; (d) relative tangential velocity along the surface streamline. ($\dot{m}_o$ = 30 mg/s, Ω = 2000 rad/s, $\alpha_i = 6°$, $T_{t,i}$ = 313 K, Δ_{rc} = 0.2 mm.)

An interesting flow feature can be most clearly observed in the U_r-contour for the 2-inlet configuration. It is found that the mass flow rate at the rotor exit is not axisymmetric; the most interesting feature of this circumferential variation is that the locations of the greatest mass flow rate at exit do not fall on the radial lines extended from the inlets but are situated somewhere in between the radial positions of two consecutive inlets. Transport of mass by the significant amount of tangential motion is responsible for this phenomenon.

Figure 4 and several subsequent figures use the concept of surface streamlines. The surface streamlines are constructed on a chosen plane surface from the components of in-plane velocity, i.e., by not considering the velocity component which is perpendicular to the chosen surface. All the surface streamlines shown in the present paper are constructed on a special $r-\theta$ plane which passes through $z = b/2$ (i.e., on the middle-plane of the inter-disc-spacing). For this particular surface, the surface streamlines are also the true streamlines since the out-of-plane velocity, i.e., U_z, is actually zero at $z = b/2$.

Figure 4(a) shows a surface-streamline at $z = b/2$ for a 4-inlet configuration. The surface-streamline is obtained by post-processing the velocity fields at $z = b/2$. The locations of the four inlets are indicated by roman numerals (I, II, III, and IV). The surface-streamline started at inlet-I continues up to the outlet following a nearly spiral-shaped curve. Figures 4(b)–4(d) display, respectively, the variations of $|U_r|$, U_θ, and V_θ along the surface-streamline. The wavy appearance of the curves (representing $|U_r|$, U_θ, and V_θ) arises due to the existence of non-axisymmetry in the flow field. Crests and troughs of the wavy $|U_r|$ versus r curve are indicated by numbers 1, 2, 3, ... [see Fig. 4(b)]. The same numbers are inserted in Fig. 4(a) to display the locations of these crests and troughs on the surface-streamline. It is observed that the crests appear close to the azimuthal locations of the inlets, while the troughs occur (azimuthally midway) between two consecutive inlet-nozzles. At the periphery ($r = r_i$), between two consecutive inlet-nozzles, a portion of the shroud-wall is present. The radial velocity is zero at the shroud-wall, whereas its magnitude is large at the inlet-regions. Such a non-axisymmetric condition at $r = r_i$ influences the downstream distribution of radial velocity and governs the origination of the crests and troughs.

For axisymmetric condition, U_r is not a function of θ and its magnitude increases toward the outlet according to

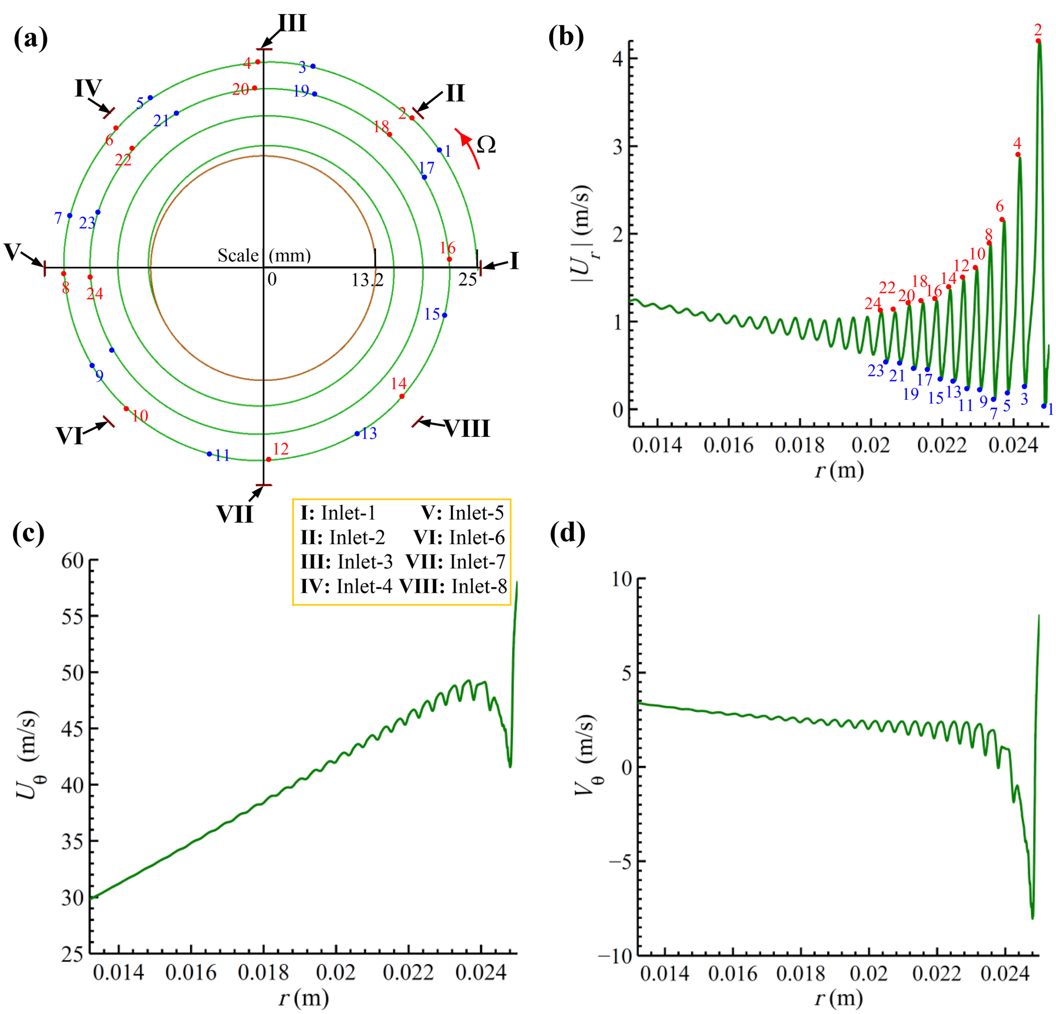

FIG. 5. Attainment of axisymmetry along a surface streamline located on the middle-plane of the inter-disc-spacing (i.e., on $z = b/2$) for an eight-inlet flow-configuration. (a) A surface streamline extending from r_d to r_o; (b) the magnitude of radial velocity along the surface streamline; (c) tangential velocity along the surface streamline; (d) relative tangential velocity along the surface streamline. ($\dot{m}_o$ = 30 mg/s, Ω = 2000 rad/s, $\alpha_i = 6^\circ$, $T_{t,i}$ = 313 K, Δ_{rc} = 0.2 mm.)

the relation $|U_r| \propto 1/r$. Figure 4(b) shows that the spatial oscillation in U_r decays in the downstream direction, whereby the crests and the troughs progressively tend to the unique line that would be obtained in the case of axisymmetric flow. In other words, there is a decay of the non-axisymmetry toward the outlet.

Figure 4(d) exhibits that in the variation of V_θ, the influence of non-axisymmetry is retained even near the outlet. Figure 4(c) exhibits that in the variation of U_θ, the influence of non-axisymmetry has disappeared within a short radial distance from $r = r_i$. It is already explained why U_θ attains axisymmetry within a short radial distance from $r = r_i$. Figure 4(c) also shows that along the surface-streamline, the wavy trend of U_θ is converted to a nearly linear trend (explanation given in the next paragraph).

Figure 5(a) shows a surface-streamline on the plane $z = b/2$ for an 8-inlet configuration. Figures 5(b)–5(d) display, respectively, the variations of $|U_r|$, U_θ, and V_θ along the surface-streamline. Near the inlet, U_θ decreases sharply [Fig. 5(c)]. It is so because Ωr decreases linearly with radius and V_θ decreases drastically [Fig. 5(d)]. In other radial locations, the magnitude of V_θ is much smaller than the magnitude of Ωr, and the change in V_θ is not drastic. Thus U_θ decreases almost linearly. It was mentioned that starting from $r = r_i$, $|U_r|$ decreases up to a certain radius, but then onward increases (up to the outlet). This flow feature is observed in Fig. 5(b) [also in Fig. 4(b)].

As the number of inlets N_{inlet} increases, the spatial oscillation in various velocity components subsides more quickly (i.e., closer to the inlet). A comparison of Figs. 4(b)–4(d), respectively, with their counterparts Figs. 5(b)–5(d) establishes this generic trend.

B. Effect of increasing rotational speed of the discs (Ω)

The effect of increasing Ω is investigated keeping all other input parameters, viz., $\dot{m}_o$, α_i, $T_{t,i}$, Δ_{rc}, and N_{inlet}, fixed. Figure 6 shows the contours of U_r on the middle-plane of the inter-disc-spacing (i.e., on $z = b/2$) for an eight-inlet flow-configuration ($N_{inlet} = 8$). Figures 6(a)–6(c) display the contours for $\Omega = 1000$ rad/s, $\Omega = 1500$ rad/s, and $\Omega = 2000$ rad/s, respectively.

At first, we focus our attention on the region near $r = r_i$, where U_r is typically non-axisymmetric because of the presence of discrete inlets. The magnitude of U_r is large adjacent to each of the inlets, and the magnitude of U_r is small between

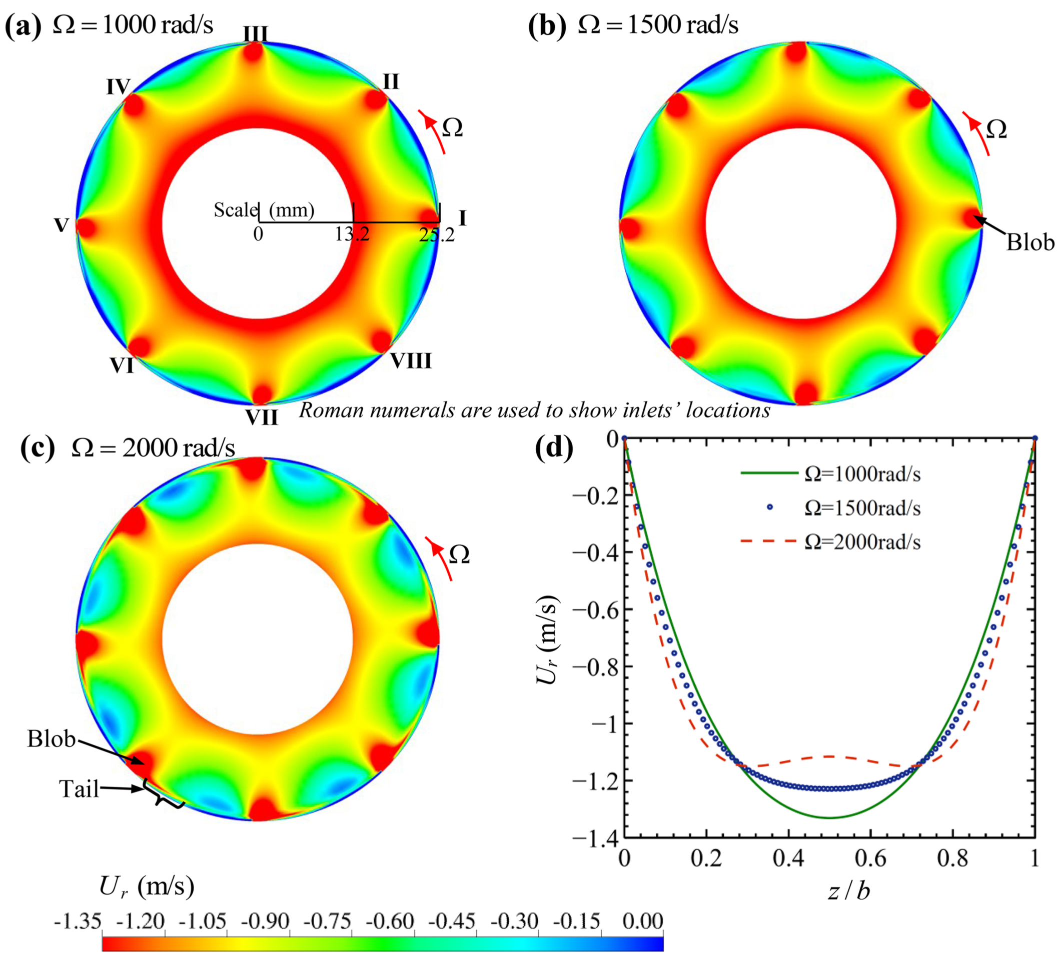

FIG. 6. Effect of increasing the rotational speed of the discs (Ω) on the radial velocity distribution. All contours are located on the middle-plane of the inter-disc-spacing (i.e., on $z = b/2$) for an eight-inlet flow-configuration. (a) Contours for $\Omega = 1000$ rad/s; (b) contours for $\Omega = 1500$ rad/s; (c) contours for $\Omega = 2000$ rad/s; (d) z-variations of U_r at $r = 15$ mm and $\theta = 0°$ obtained for the three representative values of Ω. ($\dot{m}_o = 30$ mg/s, $\alpha_i = 6°$, $T_{t,i} = 313$ K, $\Delta_{rc} = 0.2$ mm.)

two consecutive inlets. For Ω = 2000 rad/s, a portion of the large-$|U_r|$-region enters into the small-$|U_r|$-region. Due to such entrainment, the large-$|U_r|$-region looks like a blob with a tail [see Fig. 6(c)]. Such an interaction between small-$|U_r|$ and large-$|U_r|$-regions does not occur for small values of Ω. Consequently, the tail-like-feature does not appear, e.g., see Fig. 6(a) corresponding to Ω = 1000 rad/s. It has already been mentioned that at a short radial distance from $r = r_i$, $|U_r|$ decreases because of the azimuthal spreading, and U_θ also decreases and becomes of the order of Ωr. The value of Ω determines the difference between the magnitudes of U_θ and $|U_r|$ near $r = r_i$. When Ω is large, U_θ is much greater than U_r near $r = r_i$. At large values of Ω, due to the presence of a large tangential momentum, a chunk of fluid adjacent to the inlet region shifts tangentially in the direction of disc-rotation, keeping its radial momentum (which drives the fluid radially inward) intact. Such tangential shift results in the tail-like-feature.

We now focus our attention on the region near $r = r_o$. Near $r = r_o$, the distribution of U_r is more or less axisymmetric in nature, and the value of U_r (on $z = b/2$ plane) decreases with an increase in Ω. To investigate the reason of the decrease of U_r with increasing Ω, z-profiles of U_r are calculated at various Ω. Figure 6(d) shows the z-profiles obtained at r = 15 mm and $\theta = 0°$ for the three different values of Ω. When Ω = 1000 rad/s, the z-variation is parabolic in nature. In the parabolic distribution, the maximum value occurs at $z = b/2$. When Ω = 1500 rad/s, the z-profile is no longer parabolic. A flat trend is attained near $z = b/2$. With a further increase in Ω, a W-shaped profile is obtained, e.g., see the profile corresponding to Ω = 2000 rad/s. In such W-shaped profiles, two maxima exist while there is a minima at the centreline. The transition from the parabolic to flat to the W-shaped profiles explains why, with increasing Ω, the magnitude of U_r at the centreline decreases near the outlet.

The formation of the W-shaped profiles can be explained as follows. Near the outlet of the representative 8-inlet configuration, axisymmetry is nearly attained and the Mach number remains below 0.3. We, therefore, consider the continuity equation for steady, laminar, axisymmetric, and incompressible flow,

$$\frac{1}{r}\frac{\partial (rU_r)}{\partial r} + \frac{\partial U_z}{\partial z} = 0. \tag{7}$$

An integral form of Eq. (7) is

$$-U_r = \frac{\int (\partial U_z/\partial z)\, r\delta r}{r} + \frac{c(z)}{r}. \tag{8}$$

The contributions of the viscous effect and total inertia (comprising inertia, Coriolis, and centrifugal terms) in the radial momentum equation would change with a change in Ω.[1] In the subsequent discussion, the total inertia is called inertia for simplicity. When Ω is small, the viscous effect dominates over the inertial effect and the pressure gradient term in the radial momentum equation is principally balanced by the viscous term. The $U_r - z$ profile is then found to be parabolic. Reference 7 shows that when the parabolic profile is a good approximation, the term $(\partial U_z/\partial z)$ can be neglected. With an increase in Ω, as the inertial effect increases, the first term in the R.H.S. of Eq. (8) is no longer negligible. At the middle-plane of the inter-disc-spacing (i.e., on $z = b/2$), where the viscous effect is expected to be the smallest, this term perturbs the profile considerably. On the other hand, near the disc-surfaces, this term perturbs the profile to a smaller extent. Thus a W-shaped profile is obtained for a large value of Ω.

It has already been shown that near the outlet ($r = r_o$), the z-profiles of U_r are parabolic for comparatively small values of Ω (e.g., Ω = 1000 rad/s). However, even when Ω is small, the z-profiles of U_r may not be parabolic near $r = r_i$ as a consequence of the non-axisymmetry introduced by the presence of multiple discrete inlets.

A comparison of Figs. 6(a)–6(c) shows that the approach to axisymmetry in the radial velocity U_r is delayed (i.e., the radial location moves toward the outlet) as the rotational speed Ω is increased. Similar results (not displayed here) for relative tangential velocity V_θ and static pressure p show that the amplitudes of fluctuations in these quantities at a given radial location increase with increasing Ω. However, when these amplitudes are normalized by the average values of the respective quantities at the same radial location, the resulting normalized fluctuations are found to decrease marginally with increasing Ω. The normalized fluctuation in U_r at any radial location, on the other hand, increases with increasing Ω.

The progressive development of the z-profiles of U_r is examined along a surface streamline located on the middle-plane of the inter-disc-spacing and constructed from $r = r_i$ to $r = r_o$. The streamline is shown in Fig. 7. There are 20 red dots shown on the streamline indicating 20 special locations on the $\theta - r$ plane at which the z–profiles of U_r are determined. These profiles are organized in ten sub-plots. (Note that the ordinates of the velocity profiles use two different scales—one for points 1-8 and the other for points 9-20). The profiles at odd-numbered locations (e.g., 1, 3, and 5, etc.), which represent the azimuthal positions of the inlets, are shown by dotted lines. The profiles at even-numbered locations (e.g., 2, 4, and 6, etc.), which represent the azimuthal midpoints between two consecutive inlets, are shown by solid lines. The figure shows that with decreasing radius, the profiles change from W-shaped to flat to parabolic. The velocity at $z = b/2$ at the even-numbered locations (solid lines) seems to increase continuously from the inlet to exit. The velocity at $z = b/2$ at the odd-numbered locations (dotted lines) decreases at first and then onward increases as one moves from the inlet to exit. The difference between the solid and the dotted lines decreases with a decrease in radius, indicating the progressive attainment of an axisymmetric condition. When axisymmetry is almost attained, the magnitude of U_r along both solid and dotted lines increases (see curves 15-20) due to the progressive decrease of the flow cross-sectional area.

It is to be noted that results for Ω = 1000 rad/s are shown in Fig. 7. Results for a range of rotational speeds, depicted in Fig. 6, show that the $U_r - z$ profile near the outlet can be W-shaped when Ω is large. Thus the evolution of particular shapes (W-shaped to flat to parabolic) shown in Fig. 7 may not be obtained at higher rotational speeds; the progressive approach of the two sets of profiles (shown by dotted and solid lines) to each other still occurs in the process of attainment of the axisymmetric condition.

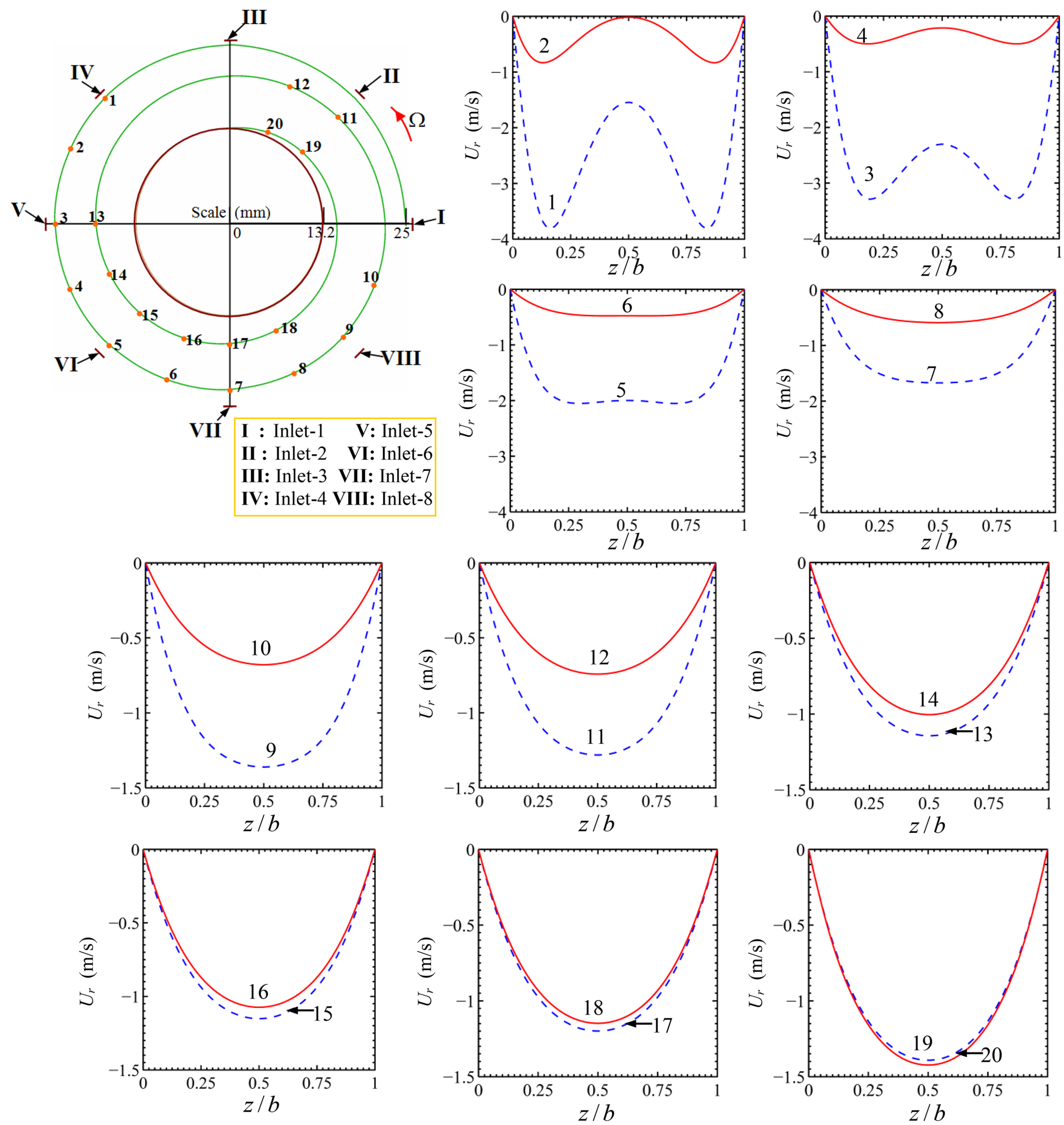

FIG. 7. Progressive development of the z-profiles of U_r along a surface streamline located on the middle-plane of the inter-disc-spacing for an eight-inlet flow-configuration. (The dots on the streamline indicate the locations where the profiles are presented. Blue dotted lines indicate velocity profiles at points whose azimuthal positions are directly aligned with the inlets, and red solid lines indicate velocity profiles at points which fall in the middle of two consecutive inlets. Note that the ordinates of the velocity profiles use two different scales—one for points 1-8 and the other for points 9-20. Simulation is performed for $\dot{m}_o$ = 30 mg/s, Ω = 1000 rad/s, α_i = 6°, $T_{t,i}$ = 313 K, Δ_{rc} = 0.2 mm.)

C. Effect of radial clearance (Δ_{rc}) on the velocity distribution

CFD simulations are performed for both Δ_{rc} = 0 and $\Delta_{rc} \neq 0$. Representative results are shown in this section for a 2-inlet configuration (N_{inlet} = 2). Figure 8 shows the effect of radial clearance on the contours of absolute tangential velocity near the inlet. Figure 8(a) corresponds to Δ_{rc} = 0 and Fig. 8(b) corresponds to Δ_{rc} = 0.2 mm. For both cases, from inlet-I, the tangential component of fluid's momentum is transported in the θ-direction along the shroud wall. For Δ_{rc} = 0.2 mm, the large valued contour-band, starting from inlet-I, is extended almost up to inlet-II, whereas for Δ_{rc} = 0, the large valued contour-band disappears well before inlet-II.

Figure 9 shows the effect of radial clearance on the distributions of radial velocity. Figure 9(a) corresponds to Δ_{rc} = 0 and Fig. 9(b) corresponds to Δ_{rc} = 0.2 mm. For Δ_{rc} = 0, the radial velocity (U_r) is typically non-axisymmetric near the outlet. It is observed that the azimuthal location of the large-U_r-zone near exit is offset by about 45° (for the case of two inlets) from the azimuthal location of inlet-I in the direction of disc rotation. High absolute tangential velocity near inlet-I drives the fluid in the direction of disc rotation, and the radial entry of the fluid into the inter-disc-spacing is affected by the distribution of absolute tangential velocity along the rotor's periphery. For Δ_{rc} = 0.2 mm, it can be observed that the radial velocity is almost axisymmetric near the outlet. The axisymmetry of radial velocity near the outlet is attained due to the nearly axisymmetric distribution

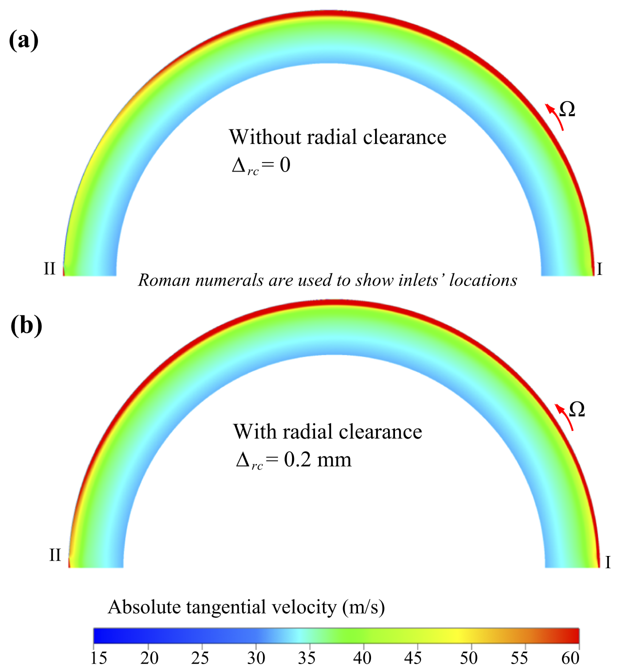

FIG. 8. Effect of radial clearance on the distributions of absolute tangential velocity near the inlet. (a) Without radial clearance ($\Delta_{rc} = 0$); (b) with radial clearance ($\Delta_{rc} = 0.2$ mm). ($N_{inlet} = 2$, $\dot{m}_o = 30$ mg/s, $\Omega = 1500$ rad/s, $\alpha_i = 6°$, $T_{t,i} = 313$ K.)

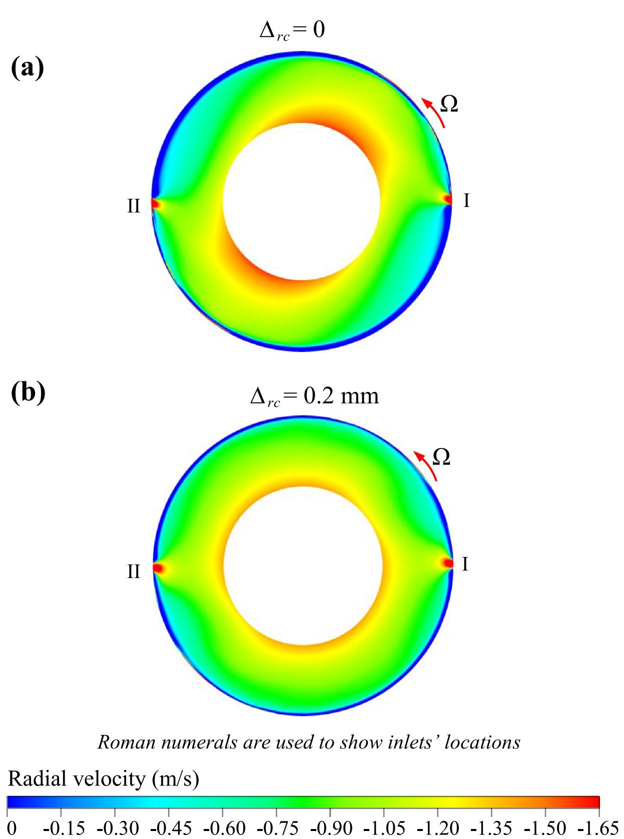

FIG. 9. Effect of radial clearance on the distributions of radial velocity. (a) Without radial clearance ($\Delta_{rc} = 0$); (b) with radial clearance ($\Delta_{rc} = 0.2$ mm). ($N_{inlet} = 2$, $\dot{m}_o = 30$ mg/s, $\Omega = 1500$ rad/s, $\alpha_i = 6°$, $T_{t,i} = 313$ K.)

of absolute tangential velocity [Fig. 8(b)] along the rotor's periphery.

In brief, an increase in the radial clearance Δ_{rc} from zero to a finite value assists in the attainment of the axisymmetric condition for both tangential and radial velocities, i.e., the axisymmetry is obtained at a larger radial location. With suitable combinations of N_{inlet}, Ω, and Δ_{rc}, the axisymmetry in absolute tangential velocity may be obtained quite close to the inlet itself, whereas the non-axisymmetry in radial velocity persists much longer along the flow path and axisymmetry is approached (for the adopted geometry) only near the outlet, if at all.

1. Fluid dynamics inside the radial clearance space between the rotor and the shroud

The radial clearance space refers to the region between r_i and r_d. The difference of r_i and r_d, i.e., $(r_i - r_d) \equiv \Delta_{rc}$, is small compared to the radii r_i and r_d. The fluid dynamics in the radial clearance space is complex since the fluid has to negotiate with two different non-uniformities within a short radial distance (Δ_{rc}). At $r = r_i$, a source of non-uniformity is present in the θ–direction, depending on the number and arrangement of the discrete inlets in the circumferential plane of the stationary shroud. At $r = r_d$, a z–directional non-uniformity exists due to the presence of two closely spaced disc-surfaces (on which the boundary condition $U_\theta = \Omega r$ is imposed as a result of no slip). The contours of U_θ on various $r - z$ planes between any two inlets are constructed in Fig. 10, which, among other things, exhibit how the two above-mentioned non-uniformities govern the (rather dramatic) three-dimensional evolution of the locations of the large-U_θ and small-U_θ zones in the small clearance space.

For an 8-inlet flow-configuration ($N_{inlet} = 8$), the azimuthal extent of inlet-I is $-2° \le \theta \le 2°$, and the azimuthal extent of inlet-II is $43° \le \theta \le 47°$. In the space between inlet-I and inlet-II, eight representative r-z planes, viz., P1, P2, ..., P8, are chosen. Figure 10 shows these eight r-z planes and the distribution of absolute tangential velocity on these eight planes. It has been observed that the contours are symmetric about the mid-plane of the inter-disc-spacing; therefore, we have shown only the upper half, i.e., from the upper disc-surface up to the mid-plane. $z = 0.3$ mm and $z = 0.15$ mm indicate the locations of upper disc-surface and mid-plane of the inter-disc-spacing, respectively.

On the stationary wall of the shroud (at $r = 25.2$ mm), no slip boundary condition is specified. The contours on P2, P3, ..., P8 exhibit the presence of a boundary-layer developed near the shroud-wall. The stationary wall is absent within the region $-2° \le \theta \le 2°$, where the boundary layer vanishes (see the contours on P1). Figure 10 shows that the large-U_θ-zone changes its location with an increase in θ from $\theta = 0°$. The following three features pertaining to the location-change of the large-U_θ-zone are mentionable. (i) From $\theta = 0°$ to $\theta = 5°$, the large-U_θ-zone is shifted radially inward. This happens due to the sudden appearance of boundary layer near the shroud-wall. The growth of the boundary layer pushes the large-U_θ-zone further in the inward radial direction (see the contours corresponding on P2, P3, and P4). (ii) From $\theta = 15°$ to $\theta = 30°$, the z–extent of the large-U_θ-zone diminishes and exists near

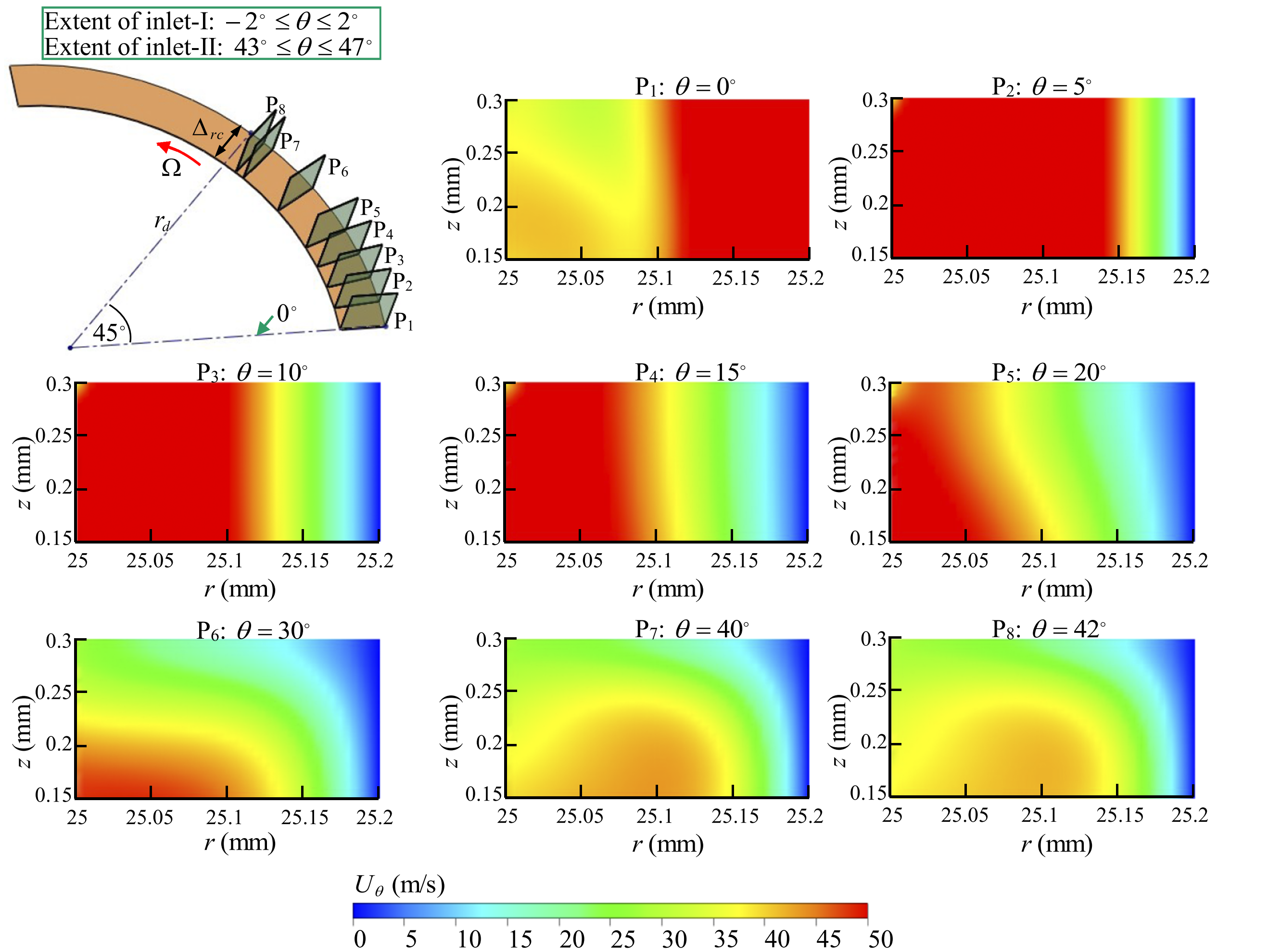

FIG. 10. Distribution of tangential velocity within the small radial clearance between the rotor (up to r = 25 mm) and the shroud-wall (at r = 25.2 mm). z = 0.3 mm and z = 0.15 mm indicate the locations of upper disc and mid-plane of the inter-disc-spacing, respectively. (N_{inlet} = 8, $\dot{m}_o$ = 30 mg/s, Ω = 1200 rad/s, $\alpha_i = 6^\circ$, $T_{t,i}$ = 313 K, Δ_{rc} = 0.2 mm.)

the centre of inter-disc-spacing (see the contours on P4, P5, and P6). (iii) From $\theta = 30^\circ$ to $\theta = 42^\circ$, the large-U_θ-zone, while diminished in magnitude, gets shifted radially outward from r = 25 mm to r = 25.1 mm (see the contours on P6, P7, and P8). The value of U_θ at disc-surfaces ($U_\theta = \Omega r_d$), set by the no-slip boundary condition, is smaller than the value of U_θ at inlet. Viscous dissipation initiated at the disc surface (present at z = 0.3 mm) is responsible for the fluid dynamic features described in observations (ii) and (iii) mentioned above.

IV. CONCLUSION

The paper presents a systematic computational study of the flow in a shrouded rotor cavity (with depth of the order of 100 μm) with multiple discrete inflows revealing the physics of how an initially non-axisymmetric flow evolves, both in the Lagrangian and Eulerian frameworks, towards axisymmetry. The fluid dynamics is studied by varying the number of inlets (N_{inlet}), rotational speed of the discs (Ω), and radial clearance between the rotor and the shroud (Δ_{rc}), while keeping the inlet mass flow rate, total temperature, and flow angle fixed.

When the number of inlets N_{inlet} is increased, keeping all other input parameters fixed, the flow condition at the rotor's inlet becomes more uniform which assists in the attainment of axisymmetric condition in the tangential and radial velocities, i.e., the axisymmetry is obtained at a larger radial location. Of the two components of the absolute tangential velocity U_θ, the relative tangential velocity V_θ depends on θ but Ωr is independent of θ. For the adopted geometry and input parameters, V_θ decreases substantially near the inlet, and Ωr becomes the dominant part of U_θ. Although the non-axisymmetry in V_θ persists much longer along the flow path, axisymmetry in U_θ is approached much earlier (i.e., at a larger radial location) due to the contribution of Ωr.

The non-uniform inlet condition for the radial and tangential velocities, consisting of high velocity at the inlet openings and zero velocity on the shroud wall in between two consecutive inlets, gives rise to an oscillatory variation in the velocity of a fluid particle if one tracks its motion along a surface streamline [Figs. 4(a) and 5(a)]. The amplitude of oscillation in the radial velocity (U_r) is much larger than that in the tangential velocity (either U_θ or V_θ) and the oscillation in U_r persists much longer along the spiral flow path. It is found that the crests of the fluctuating velocities (at various turns of the spiral path) repeatedly occur close to the azimuthal positions of the inlets, whereas the troughs occur close to the azimuthal mid-points between two consecutives inlets. The amplitude of the fluctuations progressively decreases; this feature in the Lagrangian description is directly related to the approach to axisymmetric condition in the Eulerian description of the velocity field. The rate of decay of the amplitude increases, i.e., equivalently the approach to the axisymmetric condition happens at a greater radial location as the number of inlets N_{inlet} is increased.

When the rotational speed of the discs (Ω) is changed keeping all other input parameters fixed, the distribution of radial velocity is significantly altered, which may result even in a change of the fundamental shape of its z-profile. At small Ω, the maximum outflow occurs at the middle plane between the two discs; whereas at large Ω, the maximum outflow occurs at two separate planes offset from the middle plane. Thus with increasing Ω, the z-profile of radial velocity changes from parabolic to flat to W-shaped (Fig. 6). This important and interesting effect of Ω on the fundamental shape of the z-profile of U_r has not been described in the previous literature.

The fluid dynamics in the radial clearance space is complex since the fluid has to negotiate with two different non-uniformities within a short radial distance (Δ_{rc}). At $r = r_i$, a source of non-uniformity is present in the θ–direction, depending on the number and arrangement of the discrete inlets in the circumferential plane of the stationary shroud. At $r = r_d$, a z–directional non-uniformity exists due to the presence of two closely spaced disc-surfaces (on which the boundary condition $U_\theta = \Omega r$ is imposed as a result of no slip). The contours of U_θ on various $r - z$ planes between any two inlets, constructed in Fig. 10, exhibit how the two above-mentioned non-uniformities govern the rather dramatic three-dimensional evolution of the locations of the large-U_θ and small-U_θ zones in the small radial clearance space.

An increase in the radial clearance Δ_{rc} from zero to a finite value assists in the attainment of axisymmetric condition for both tangential and radial velocities, i.e., the axisymmetry is obtained at a larger radial location. With suitable combinations of N_{inlet}, Ω, and Δ_{rc}, the axisymmetry in absolute tangential velocity may be obtained quite close to the inlet itself, whereas the non-axisymmetry in radial velocity persists much longer along the flow path and axisymmetry is approached (for the adopted geometry) only near the outlet, if at all.

The subtle and complex fluid dynamics of the approach to axisymmetry is comprehensively analysed in Fig. 7 by following the progressive development of the z-profiles of U_r along a surface streamline located on the middle-plane of the inter-disc-spacing for an eight-inlet flow-configuration. Two sets of velocity profiles are recorded—the first set at points whose azimuthal positions are directly aligned with the inlets, and the second set at points which fall in the middle of two consecutive inlets. Both sets are of W-shape near the disc periphery, then they become flat in the middle, finally becoming parabolic (the particular shapes may be different at higher Ω). The maximum velocity in the first set decreases at first due to spreading in the azimuthal direction and then increases due to the decrease of flow cross-sectional area. The maximum velocity in the second set increases monotonically. The velocity profiles of the two sets approach each other and finally become superposed when axisymmetry is attained.

[1] A. Guha and S. Sengupta, "The physics of pressure variation in microchannels within corotating or static discs," Phys. Fluids **28**(10), 103601-1–103601-19 (2016).
[2] A. Guha and S. Sengupta, "The fluid dynamics of work transfer in the non-uniform viscous rotating flow within a Tesla disc turbomachine," Phys. Fluids **26**(3), 033601-1–033601-27 (2014).
[3] A. Guha and S. Sengupta, "The fluid dynamics of the rotating flow in a Tesla disc turbine," Eur. J. Mech. B/Fluids **37**, 112–123 (2013).
[4] B. Herrmann-Priesnitz, W. R. Calderón-Muñoz, E. A. Salas, A. Vargas-Uscategui, M. A. Duarte-Mermoud, and D. A. Torres, "Hydrodynamic structure of the boundary layers in a rotating cylindrical cavity with radial inflow," Phys. Fluids **28**(3), 033601-1–033601-16 (2016).
[5] Y. Omi and R. Iwatsu, "Numerical study of swirling flows in a cylindrical container with co-/counter-rotating end disks under stable temperature difference," Int. J. Heat Mass Transfer **48**(23), 4854–4866 (2005).
[6] A. Guha and S. Sengupta, "Similitude and scaling laws for the rotating flow between concentric discs," Proc. Inst. Mech. Eng., Part A **228**(4), 429–439 (2014).
[7] S. Sengupta and A. Guha, "A theory of Tesla disc turbines," Proc. Inst. Mech. Eng., Part A **226**(5), 650–663 (2012).
[8] S. D. Abrahamson, J. K. Eaton, and D. J. Koga, "The flow between shrouded corotating disks," Phys. Fluids A **1**(2), 241–251 (1989).
[9] C. A. Schuler, W. Usry, B. Weber, J. A. C. Humphrey, and R. Greif, "On the flow in the unobstructed space between shrouded corotating disks," Phys. Fluids A **2**(10), 1760–1770 (1990).
[10] R. F. Huang and M. K. Hsieh, "Phase-resolved flow characteristics between two shrouded co-rotating disks," Exp. Fluids **51**(6), 1529–1547 (2011).
[11] S. C. Wu, "A PIV study of co-rotating disks flow in a fixed cylindrical enclosure," Exp. Therm. Fluid Sci. **33**(5), 875–882 (2009).
[12] C. Y. Soong, C. C. Wu, T. P. Liu, and T. P. Liu, "Flow structure between two co-axial disks rotating independently," Exp. Therm. Fluid Sci. **27**(3), 295–311 (2003).
[13] F. Hendriks, "On Taylor vortices and Ekman layers in flow-induced vibration of hard disk drives," Microsyst. Technol. **16**(1-2), 93–101 (2010).
[14] K. Shirai, Y. Yaguchi, L. Büttner, J. Czarske, and S. Obi, "Highly spatially resolving laser Doppler velocity measurements of the tip clearance flow inside a hard disk drive model," Exp. Fluids **50**(3), 573–586 (2011).
[15] N. Tesla, Turbine U.S. patent 1 061 206 (1913).
[16] G. P. Hoya and A. Guha, "Design of a test rig and study of the performance and efficiency of a Tesla disc turbine," Proc. Inst. Mech. Eng., Part A **223**(4), 451–465 (2009).
[17] A. Guha and B. Smiley, "Experiment and analysis for an improved design of the inlet and nozzle in Tesla disc turbines," Proc. Inst. Mech. Eng., Part A **224**(2), 261–277 (2010).
[18] A. Guha and S. Sengupta, "A non-dimensional study of the flow through co-rotating discs and performance optimization of a Tesla disc turbine," Proc. Inst. Mech. Eng., Part A (published online 2017).
[19] O. Czarny, H. Iacovides, and B. E. Launder, "Precessing vortex structures in turbulent flow within rotor-stator disc cavities," Flow, Turbul. Combust. **69**(1), 51–61 (2002).
[20] C. Nore, M. Tartar, O. Daube, and L. S. Tuckerman, "Survey of instability thresholds of flow between exactly counter-rotating disks," J. Fluid Mech. **511**, 45–65 (2004).
[21] R. E. Hewitt and M. Al-Azhari, "Non-axisymmetric self-similar flow between two rotating disks," J. Eng. Math. **63**(2-4), 259–277 (2009).
[22] ANSYS CFX 15, Theory Guide of ANSYS CFX 15, ANSYS, Inc., Canonsburg, PA 15317, USA, 2013.
[23] C. M. Rhie and W. L. Chow, "A numerical study of the turbulent flow past an isolated airfoil with trailing edge separation," AIAA Paper No. 82–0998, 1982.
[24] Y. Mei and A. Guha, "Implicit numerical simulation of transonic flow through turbine cascades on unstructured grids," Proc. Inst. Mech. Eng., Part A **219**(1), 35–47 (2005).